ACS APPLIED MATERIALS & INTERFACES

Research Article

www.acsami.org

High-Performance Zn−TiC−C Nanocomposite Alloy Anode with Exceptional Cycle Life for Lithium-Ion Batteries

Sang-Ok Kim and Arumugam Manthiram*

Materials Science and Engineering Program and Texas Materials Institute, The University of Texas at Austin, Austin, Texas 78712, United States

Supporting Information

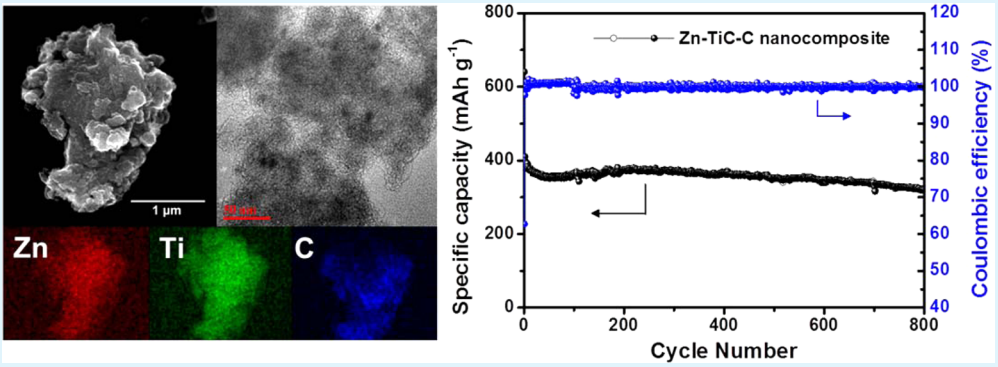

ABSTRACT: A Zn-based nanocomposite has been prepared through a facile, low-cost high-energy mechanochemical process and employed as an anode material for lithium-ion batteries. Structural characterization reveals that the micrometer-sized Zn−TiC−C nanocomposite is composed of Zn nanocrystals uniformly dispersed in a multifunctional TiC and conductive carbon matrix with a tap density of 1.3 g cm^{-3}. The Zn−TiC−C nanocomposite exhibits high reversible volumetric capacity (468 mA h cm^{-3}), excellent cyclability over 800 cycles (79.2% retention), and good rate performance up to 12.5C (75% of its capacity at 0.25C rate). The enhanced electrochemical performance is mainly due to the presence of the well-mixed TiC + C matrix that plays an important role in providing high conductivity as well as mechanical buffer that mitigates the huge volume expansion and contraction during prolonged cycling. In addition, it prevents the particle growth by uniformly dispersing nanosized Zn within itself during cycling, maintaining high utilization (∼100%) and fast reaction kinetics of Zn anode.

KEYWORDS: *lithium-ion batteries, anode, zinc, titanium carbide, mechanical milling*

1. INTRODUCTION

Over the past few decades, lithium-ion batteries (LIBs) have played a crucial role in powering a variety of consumer electronics owing to their high energy density, long cycle life, and low self-discharge rate.[1,2] Recently, with the rapid growth of emerging technologies such as electric vehicles and grid-scale energy storage systems, there has been great interest in developing high capacity electrode materials with a focus on high rate capability, good safety, and affordability. Currently, graphite is the most widely used anode material for LIBs, but it has major drawbacks including relatively low theoretical specific capacity (LiC_6: 372 mA h g^{-1}), poor rate capability, and severe safety issues associated with Li plating.[3,4] Enormous efforts have been dedicated to replace graphite with high capacity Li-alloy systems based on Li−Si,[5−7] Li−Sn,[8,9] and Li−Sb[10−12] alloying reactions in order to satisfy the ever-increasing demand for high performance LIB systems.

Elemental Zn is one of the alternative Li-alloy based materials. Even though it has a relatively low theoretical gravimetric capacity (LiZn: 410 mA h g^{-1}) which is only slightly greater (∼10%) than graphite, it has several advantages such as high volumetric capacity (1511 mA h cm^{-3}) and low operating voltage of mainly <0.4 V (vs Li/Li^+). Other beneficial features including inexpensiveness, natural abundance, and eco-friendliness make it a desirable and promising candidate to be used as an anode material in LIBs.[13] Despite these merits, Zn has not attracted great attention because it also inevitably suffers from volume change of active particles during the Li insertion and extraction processes and particle agglomeration issues upon extended cycling that eventually result in the severe capacity fading and poor rate capability, similar to other Li-alloying materials.[14,15] Accordingly, only a few studies on the synthesis and characterization of Zn-based anode materials have been reported.[16−20] Among them, employment of a mixed Al_2O_3 and carbon as an efficient buffer matrix for Zn anode led to a relatively good cycling stability with a reversible capacity of ∼380 mA h g^{-1} after 100 cycles,[20] thereby showing the feasibility for the use of an active/inactive composite strategy.

Received: April 10, 2015
Accepted: June 22, 2015
Published: June 22, 2015

DOI: 10.1021/acsami.5b03110
ACS Appl. Mater. Interfaces 2015, 7, 14801−14807

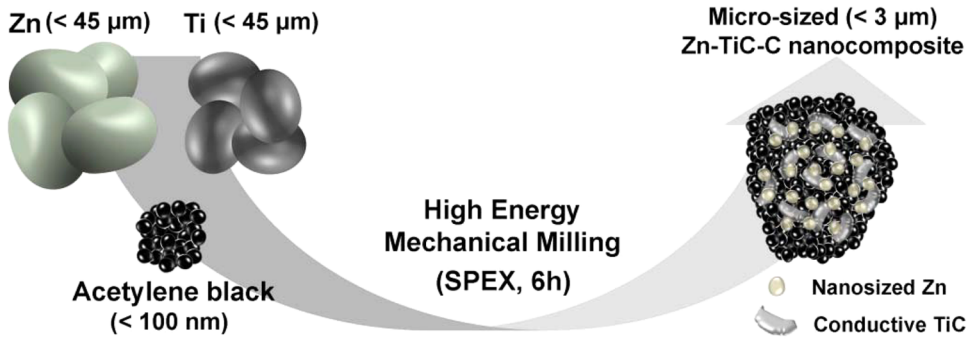

Figure 1. Schematic diagram of the preparation of the Zn−TiC−C nanocomposite.

Nonetheless, the limited cycling stability only up to 100 cycles and the low rate performance are still required to be overcome.[13]

Several recent studies have proven that the introduction of a combined TiC and conductive carbon (TiC + C) buffer is clearly beneficial to improve electrochemical performance of various Li- and Na-alloying active materials.[9,12,21−24] TiC is well-known to be stiff, electronically conductive, and electrochemically stable,[25,26] so it can be used as a structure-reinforcing buffer matrix against large volume change occurring during electrochemical cycling of nanocomposite alloy anode systems. Also, TiC buffer is much more effective for the volume expansion issue of Zn anode as Zn undergoes a relatively smaller volume expansion of ∼71% (LiZn) during lithiation compared to Si ($Li_{15}Si_4$, ∼300%), Sn ($Li_{22}Sn_5$, ∼280%), and Sb (Li_3Sb, ∼200%). Moreover, the addition of conductive carbon increases further the conductivity by maintaining an inter-particle electronic transport pathway and prevents particle aggregation by providing a stable dispersing matrix during prolonged cycling. As a result, the synergistic effects of the conductive TiC + C matrix could lead to dramatic improvement in electrochemical properties due to the enhancement in electrical conductivity, mechanical integrity, and structural stability.

In this study, we report a strategy of achieving unexpectedly improved electrochemical performance of Zn anode by a simple and facile incorporation of Zn nanoparticles into the multifunctional conductive buffer matrix composed of nanocrystalline TiC and carbon. The conductive TiC + C buffer matrix in a Zn−TiC−C nanocomposite provides (i) facile electron transport pathway that leads to rapid electrode kinetics, (ii) short diffusion distance of lithium ions through the formation of nanosized Zn particles, (iii) suppression of particle agglomeration during cycling by uniformly dispersing nanosized Zn within the matrix, (iv) mitigation of large volume change of Zn active particles, and (v) high chemical and electrochemical stability of the nanocomposite in organic electrolyte.

2. EXPERIMENTAL SECTION

2.1. Sample Preparation. The Zn−TiC−C nanocomposite was prepared by the high-energy mechanical milling (HEMM) process with a SPEX 8000M machine. Figure 1 shows the schematic diagram of the synthetic route. The precursors used were Zn (98+%, Acros Organics), Ti (99.99%, −325 mesh, Alfa Aesar), and acetylene black carbon (−200 mesh, Alfa Aesar) powders. Elemental Zn and Ti powders were mixed with an atomic ratio of 1:1, and an appropriate amount of carbon powders was added to obtain the Zn−TiC−C nanocomposite with a mass ratio of 7:3 (Zn−Ti:C). Then, the mixture was placed in a hardened stainless steel vial (80 cm^3) with hardened steel balls and sealed under an Ar atmosphere. The total amount of powder was 2.0 g, and a ball-to-powder weight ratio was fixed at 20:1. The HEMM was conducted for 6 h at room temperature. During the HEMM process, the conductive TiC phase is generated by reaction 1 below:

$$\mathrm{Zn + Ti + C \rightarrow Zn{-}TiC{-}C\ nanocomposite} \quad (1)$$

The Zn−TiC−C nanocomposite was collected and stored in a vacuum desiccator to minimize surface oxidation. For comparison, a Zn−C composite was prepared by the same method described above, without the addition of elemental Ti powder. The weight ratio of Zn and C was 7:3.

2.2. Sample Characterization. The structural properties of the Zn-based composites were investigated with a Philips X-ray diffractometer with Cu Kα (λ = 1.5418 Å) radiation and Kratos X-ray photoelectron spectroscopy (XPS). The powder morphology and the detailed microstructure of the Zn−TiC−C nanocomposite were observed with a JEOL JSM-5610 scanning electron microscopy (SEM) equipped with energy dispersive X-ray spectroscopy (EDS), JEOL 2010F high resolution transmission electron microscopy (HRTEM), and Hitachi S-5500 scanning transmission electron microscopy (STEM). A Quantachrome AT-4 Autotap machine was used to obtain the tap density of the samples.

2.3. Electrochemical Measurements. The electrodes were prepared by mixing slurries containing 70 wt % active material (Zn-based composites), 15 wt % Super P conducting agent, and 15 wt % polyvinylidene fluoride (PVdF) binder in *n*-methylpyrrolidinone (NMP), then coating onto a Cu foil current collector (thickness of 10 μm). After drying in a vacuum oven at 120 °C for 8 h and pressing, the disk electrodes were used to fabricate the CR2032 type coin cells for electrochemical tests. The test cells were assembled in an Ar-filled glovebox including a polypropylene (Celgard 2500) separator and a Li foil counter electrode. The electrolyte used was 1 M $LiPF_6$ dissolved in ethylene carbonate (EC)/diethyl carbonate (DEC) (50:50 vol %). The electrodes used had a typical loading mass of ∼1.5 mg cm^{-2}.

The charge−discharge experiment was performed at a constant current density of 100 mA g^{-1} within a voltage range of 0.0−2.0 V (vs Li/Li^+) with an Arbin battery tester. Rate capability test was conducted at various current densities from 100 mA g^{-1} to 5 A g^{-1}. The specific capacity was obtained based on the total weight of the active materials including Zn, TiC, and carbon in the electrode. Li was inserted when discharging and extracted during charging steps. An impedance/gain-phase analyzer (Solartron SI 1260) combined with an electrochemical interface (Solartron SI 1286) was used for electrochemical impedance spectroscopy (EIS) measurements, with an ac amplitude of 5 mV within the frequency range of 100 kHz to 0.1 Hz.

3. RESULTS AND DISCUSSION

Figure 2 gives X-ray diffraction (XRD) pattern of the Zn−TiC−C nanocomposite. The broad diffraction peaks corresponding to TiC (JCPDS No. 74-7035, cubic, space group $Fm\bar{3}m$, a = 4.315 Å) can be clearly observed with the weak Zn peaks (JCPDS No. 78-7021, hexagonal, space group $P6_3/mmc$, a = 2.6591 Å and c = 4.8868 Å), revealing the presence of

DOI: 10.1021/acsami.5b03110
ACS Appl. Mater. Interfaces 2015, 7, 14801−14807

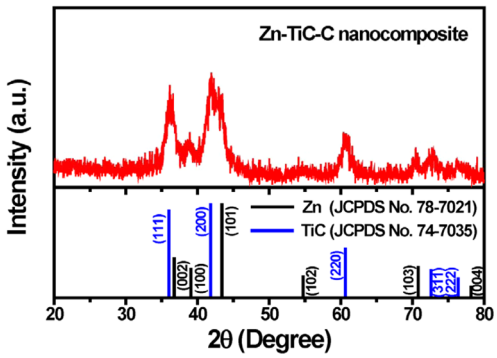

Figure 2. XRD pattern of the Zn−TiC−C nanocomposite.

conductive TiC phase along with nanosized Zn in the composite. The successful formation of conductive TiC phase is in good agreement with our previous reports on Sn- and Sb-based composite materials.[9,23] No other peaks were detected, indicating the absence of any of the Zn−Ti and Zn−C binary phases. Compared with the pure Zn precursor and the Zn−C composite (see Figure S1 in the Supporting Information), the average crystallite size of Zn in the Zn−TiC−C nanocomposite is less than ∼11 nm as evident from the further weakening and broadening of Zn diffraction peaks. The decrease in the crystallite size of Zn particle results from the successive deformation induced by HEMM with the TiC phase, which is extremely hard and strong.[25,27]

XPS measurement was conducted to characterize the binding energies of the as-synthesized Zn−TiC−C nanocomposite. The obtained XPS spectra and the corresponding curve fitting results for each element (Zn, Ti, and carbon) are given in Figure 3. The signal from Zn is deconvoluted into two peaks

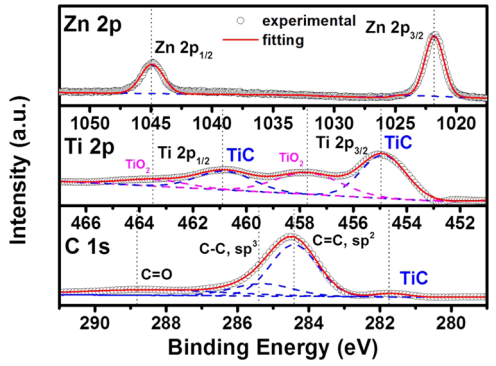

Figure 3. XPS spectra in the regions of Zn 2p, Ti 2p, and C 1s of the Zn−TiC−C nanocomposite.

located at ∼1044.8 and ∼1021.7 eV, respectively, from Zn $2p_{1/2}$ and Zn $2p_{3/2}$ as depicted in the Zn 2p spectrum, confirming that Zn does not react with either Ti or carbon during HEMM.[28] In the Ti 2p binding energy spectrum, there are two peaks from Ti $2p_{1/2}$ and Ti $2p_{3/2}$ appearing at the binding energies of ∼461.0 and ∼455.0 eV, which are higher than those from metallic Ti 2p peaks (∼459.8 and ∼453.9 eV). This indicates, in connection with a weak C 1s peak positioned at ∼281.7 eV assigned to carbide, the formation of the TiC phase in the resulting nanocomposite powders.[9,29] Two additional broad peaks located at ∼463.6 and ∼457.9 eV, with a binding energy difference (ΔE) of 5.7 eV, could be identified as TiO_2,[30,31] possibly formed by air exposure.[32,33] However, the absence of TiO_2 peaks in the XRD pattern (Figure 2) suggests that TiO_2 exists as a thin passivation layer only on the surface of the Zn−TiC−C nanocomposite and the amount of formed TiO_2 is negligible.[34] In addition, three peaks at ∼288.3 (C═O), ∼285.4 (C−C, sp^3), and ∼284.5 eV (C═C, sp^2) in the C 1s spectrum can be explained by the excess amount of carbon that remains unchanged after HEMM.[35,36] On the basis of the XRD pattern and the XPS spectra discussed above, the Zn−TiC−C nanocomposite is expected to be composed of nanosized Zn, nanocrystalline or weakly crystalline TiC, and carbon phases.

Powder morphology, microstructure, and elemental distribution of the Zn−TiC−C nanocomposite were analyzed by SEM, HRTEM, and STEM. Figure 4a shows the SEM image of the

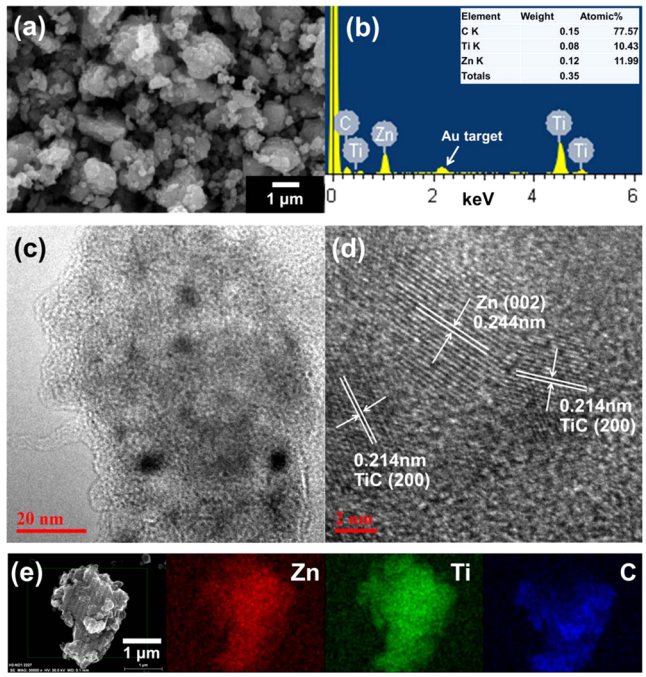

Figure 4. (a) SEM image, (b) EDS spectrum, (c) TEM, (d) HR-TEM, and (e) STEM images of the Zn−TiC−C nanocomposite. In STEM, the corresponding EDS mapping images of each element are indicated (Zn, red; Ti, green; carbon, blue).

Zn−TiC−C nanocomposite. The particle sizes of the Zn−TiC−C nanocomposite are generally in the range of a few micrometers, which is much smaller than that of elemental Zn and the Zn−C composite (see Figure S2 in the Supporting Information). The significant reduction in the particle size further confirms that the generation of the Zn−TiC−C nanocomposite is caused by the continuous fracture and welding during the HEMM process.[37] Moreover, these particles are thought to be formed by aggregation of nanosized composite particles. The SEM/EDS result (Figure 4b) shows that the amounts of Zn, TiC, and carbon in the Zn−TiC−C nanocomposite were, respectively, estimated to be ∼34.2, ∼28.6, and ∼37.2 wt % (see Figure S3 in the Supporting Information). The TEM and HRTEM images presented in Figure 4c and Figure 4d reveal the detailed microstructure of the Zn−TiC−C nanocomposite. It is obvious that the composite particles comprise nanocrystallites (darker area) embedded in an amorphous matrix (brighter area). The crystallite size is estimated to be less than 10 nm, consistent

DOI: 10.1021/acsami.5b03110
ACS Appl. Mater. Interfaces 2015, 7, 14801−14807

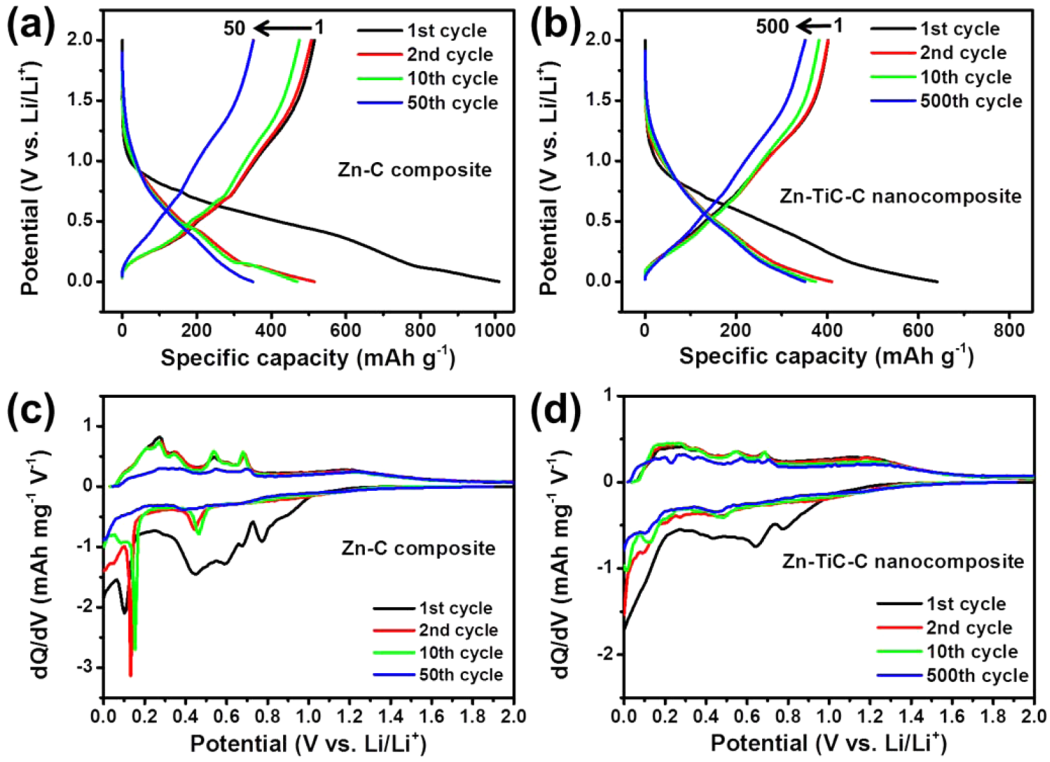

Figure 5. Voltage profiles of (a) Zn−C composite and (b) Zn−TiC−C nanocomposite and differential capacity plots of (c) Zn−C composite and (d) Zn−TiC−C nanocomposite at various cycles within a voltage window of 0.0−2.0 V (vs Li/Li^+) in 1 M $LiPF_6$ dissolved in EC/DEC (50:50 vol %) electrolyte.

with the XRD analysis as discussed above. These nanocrystallites can be indexed by lattice fringe analysis of the HRTEM image. It is clearly seen that there are two different interplanar spacings that correspond to (002) plane ($d \approx 0.244$ nm) of metallic Zn and (200) plane ($d \approx 0.214$ nm) of conductive TiC phase. Furthermore, the STEM and corresponding elemental mapping images in Figure 4e confirm the homogeneous distribution of Zn, TiC, and carbon in the nanocomposite particles. This powder morphology is considered to be quite advantageous because the enhanced powder conductivity as well as the strong buffering effect against large volume changes could be provided by the well-mixed TiC + C matrix in the nanostructured composite.

Galvanostatic charge and discharge experiments were performed within a voltage range of 0.0−2.0 V (vs Li/Li^+) in order to assess the electrochemical performance of the Zn-based electrodes. Figure 5a and Figure 5b represent the voltage profiles of the Zn−C composite and Zn−TiC−C nanocomposite electrodes at a current density of 100 mA g^{-1}. The Zn−C composite electrode shows first discharge (lithiation) and charge (delithiation) capacities of, respectively, 1011 and 515 mA h g^{-1}. The corresponding Coulombic efficiency (CE) is very low (~51.0%), which is comparable to the case of pure Zn (~51.8%) (see Figure S4 in the Supporting Information). In contrast, the first lithiation and delithiation capacities of the Zn−TiC−C nanocomposite electrode are, respectively, 641 and 402 mA h g^{-1}, with a higher initial CE of ~62.7%. Considering that TiC is electrochemically inactive toward Li,[21,24,26] the initial capacity loss is mainly caused by the irreversible reaction of Zn with Li. Therefore, the Zn−TiC−C nanocomposite is expected to exhibit improved reversibility because the introduction of the conductive TiC phase reduces the percentage of active Zn in the composite. After the first cycle, although the Zn−C composite exhibits a gradual decrease in reversible capacity during the initial 50 cycles, an excellent capacity retention can be observed for the Zn−TiC−C nanocomposite, as indicated by the fact that the voltage profile patterns remain quite similar over 500 cycles.

To better understand the reaction mechanism of Zn with Li in the Zn−TiC−C nanocomposite, the differential capacity plots (DCPs) of the Zn-based electrodes at various cycle numbers are presented in Figure 5c and Figure 5d. The DCP curve of the pure Zn electrode (see Figure S4 in the Supporting Information) is used to investigate electrochemical reactions between Zn and Li. During the first discharge process, it displays three peaks at ~0.7, ~0.4, and ~0.12 V, which are associated with, respectively, the formation of solid−electrolyte interphase (SEI) layer on the surface of active material and the sequential lithiation reactions of Zn, eventually forming the LiZn phase ($Zn \rightarrow LiZn_4 \rightarrow LiZn$).[18,20] Upon first charge, four reaction peaks are seen at ~0.28, ~0.33, ~0.55, and ~0.68 V, which are indicative of the successive delithiation processes from LiZn to Zn ($LiZn \rightarrow Li_2Zn_3 \rightarrow LiZn_2 \rightarrow LiZn_4 \rightarrow Zn$).[20] As shown in Figure 5c, although these peaks are not clearly observed for the Zn−C composite electrode in the first discharge step, the presence of four peaks during charging confirms the occurrence of the above-mentioned Li−Zn reactions. The large and broad peaks (0.3−1.0 V) are arising from the irreversible reaction of Li with the excess amount of carbon, and this is expected to mainly contribute to the large capacity loss in the first cycle, in conjunction with the SEI formation.[9,12] The Zn−C composite shows the Li−Zn reaction peaks at ~0.4 and ~0.12 V from the second cycle, but they no longer appear after 50 cycles, indicating the poor reversibility and low electrochemical stability of the active Zn in the Zn−C composite. This is believed to be ascribed to the aggregation of

DOI: 10.1021/acsami.5b03110
ACS Appl. Mater. Interfaces 2015, 7, 14801−14807

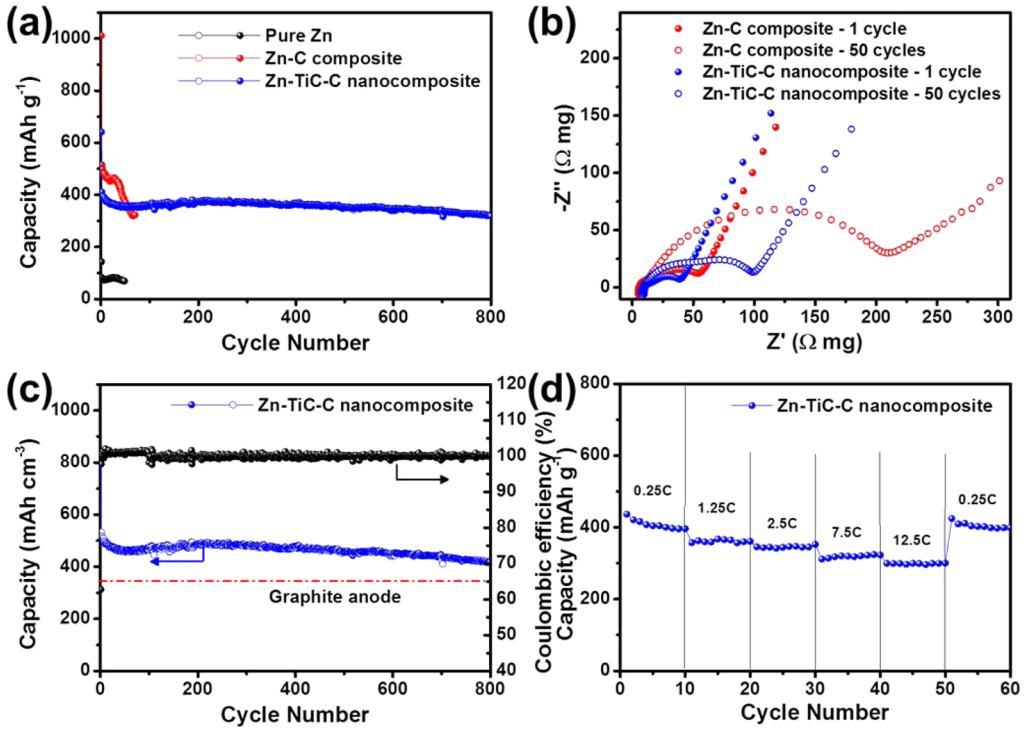

Figure 6. (a) Cycle performance of the pure Zn, Zn−C, and Zn−TiC−C nanocomposite electrodes. The specific capacity was calculated based on the total mass of active materials. (b) Nyquist plots of the Zn−C and Zn−TiC−C nanocomposite electrodes after 1 and 50 cycles. (c) Variation of the volumetric capacity and corresponding Coulombic efficiency as a function of cycle number and (d) rate capability of the Zn−TiC−C nanocomposite electrode at various current densities (1C = 400 mA g^{-1}). Note that the specific capacity and tap density of graphite in (c) are assumed to be, respectively, 350 mA h g^{-1} and 1.0 g cm^{-3}.

Table 1. Electrochemical Data of the Zn-Based Electrodes

electrode	1st discharge capacity (mA h g^{-1})	1st charge capacity (mA h g^{-1})	1st Coulombic efficiency (%)	capacity retention (*n*th/1st charge capacity) (%)
pure Zn	143	74	51.9	92.1 (*n* = 50)
Zn−C composite	1011	515	51.0	65.4 (*n* = 60)
Zn−TiC−C nanocomposite	641	402	62.7	79.2 (*n* = 800)

Zn particles during repeated cycling that is vulnerable to particle crumbling and the ensuing electrode degradation, analogous to the other Li-alloying materials such as Sn and Sb.[9,11,12,38] In the case of the Zn−TiC−C nanocomposite (Figure 4d), all the Li−Zn alloying and dealloying reaction peaks are also observable. Nevertheless, the DCP profiles are rather smooth and show much broader reaction peaks, revealing the generation of Zn nanocrystllites in the Zn−TiC−C nanocomposite as a result of the HEMM process. Moreover, the active Zn nanoparticles in the Zn−TiC−C nanocomposite still undergo reversible reaction with Li even after 500 cycles. These results demonstrate the effectiveness of TiC + C conductive matrix for the improvement of electrochemical properties by suppressing particle agglomeration and enabling high utilization of the Zn active particles.

Figure 6a illustrates and compares the cycle performance of the Zn-based electrodes at a current density of 100 mA g^{-1}. Table 1 summarizes electrochemical data of the Zn-based electrodes, including the first discharge and charge capacities, initial CE, and capacity retention after certain cycles. The pure Zn shows much lower specific capacity compared to its theoretical value (~410 mA h g^{-1}), which might be caused by the large particle size that could hinder a full lithiation process into metallic Zn particles at a relatively higher current density of 100 mA g^{-1}. The Zn−C composite exhibits significantly higher initial Li insertion and extraction capacities. This is mainly due to the formation of nanosized Zn dispersed in carbon matrix that could facilitate lithiation/delithiation processes by providing good electronic pathway among the composite particles. A reversible capacity of >450 mA h g^{-1} is maintained up to 40 cycles, but it gradually decreases to less than ~340 mA h g^{-1} after 60 cycles. On the other hand, it is remarkable to note that the Zn−TiC−C nanocomposite electrode delivers stable reversible capacity of as high as 360 mA h g^{-1} and it retains ~318 mA h g^{-1} over 800 cycles, indicating the excellent cycle performance with a high capacity retention of ~79.2%. Since the TiC phase does not react with Li, it could remain uniformly distributed in the composite even after continuous electrochemical cycling. Consequently, the TiC phase not only acts effectively as a reinforcing matrix that mitigates the volume change of the Zn active material but also provides high conductivity throughout the composite along with excess carbon, resulting in significantly enhanced cycling stability of the Zn−TiC−C nanocomposite. Considering that the reversible capacity of conductive carbon is ~480 mA h g^{-1} (see Figure S5 in the Supporting Information), the capacity contribution from Zn is estimated to be ~410 mA h g^{-1} (LiZn), which is almost the same as its theoretical value.[20] Such

DOI: 10.1021/acsami.5b03110
ACS Appl. Mater. Interfaces 2015, 7, 14801−14807

a high utilization of Zn active particles (~100%) is probably due to the nanocomposite architecture composed of a homogeneous dispersion of Zn nanoparticles within the combined highly conductive TiC + C matrix. Therefore, we could conclude that the introduction of TiC + C matrix leads to high conductivity and high reversibility of Zn anode as well as the mechanical buffering effect to alleviate the large volume changes upon extended cycling. The EIS studies (Figure 6b) further support the enhancement in the conductivity of the Zn−TiC−C nanocomposite during the electrochemical test. The difference in the charge-transfer resistance values between the Zn−C (47.2 Ω mg) and Zn−TiC−C nanocomposites (31.3 Ω mg) is rather small after the first cycle (see Figure S6 in the Supporting Information). However, the Zn−TiC−C nanocomposite (52.3 Ω mg) shows significantly lower charge-transfer resistance compared to the Zn−C composite (174.9 Ω mg) after 50 cycles, resulting from the maintenance of good electron transport path between active particles by suppressing or preventing the electrode pulverization.

Figure 6c shows the variation of the volumetric capacity and corresponding CE of the Zn−TiC−C nanocomposite electrode as a function of cycle numbers. It is generally known that graphite has a low tap density of ~1.0 g cm^{-3},[11,12] leading to a low volumetric capacity that needs to be improved. With a high tap density of ~1.3 g cm^{-3}, the Zn−TiC−C nanocomposite electrode displays a stable volumetric capacity of ~468 mA h cm^{-3}, which is ~1.35 times higher than that of graphite. The CE quickly increases to 99.9% by the fifth cycle and maintains an average value of ~99.95% through 800 cycles. Consequently, the Zn−TiC−C nanocomposite shows superior cycle performance and outperforms commercial graphite in terms of volumetric capacity that is >413 mA h cm^{-3} even after 800 cycles. In addition, electrochemical characterization is further performed at various current densities from 100 mA g^{-1} (0.25C) to 5 A g^{-1} (12.5C) (1C = 400 mA g^{-1}) to evaluate the effects of the TiC + C buffer on the rate capability of the Zn−TiC−C nanocomposite. As can be seen in Figure 6d, the Zn−TiC−C nanocomposite electrode exhibits excellent rate performance, with specific charge capacities of ~400, ~365, ~345, and ~322 mA h g^{-1}, respectively, at current densities of 0.25, 1.25, 2.5, and 7.5C rates. It is surprising that it retains a high specific capacity of ~300 mA h g^{-1} at very high current densities of as high as 12.5C, which is ~75% of its capacity at 0.25C rate. This result further suggests the facile Li^+-ion transports properties of the Zn active particles through the short diffusion path, which could be obtained by the confinement of nanosized Zn particles in the combined nanostructured TiC + C dispersing matrix that can prevent small Zn particles from aggregating into large Zn clusters even after repeated fast charge and discharge cycling.

4. CONCLUSIONS

We have successfully synthesized the Zn−TiC−C nanocomposite through a low cost, facile, high yield, and environmentally friendly HEMM process. The simple application of the well-blended TiC and carbon conductive matrix into Zn anode demonstrates superior electrochemical performance in terms of a stable reversible capacity of ~318 mA h g^{-1} with exceptionally long cycle life of over 800 cycles and high rate capability up to 12.5C rate. This dramatic performance improvement is mainly attributed to the realization of a novel nanostructured composite composed of Zn nanoparticles uniformly embedded within the TiC + C matrix. The conductive TiC + C buffer in the nanostructured Zn−TiC−C composite offers high electronic conductivity, structural reinforcement, and durable dispersing matrix that could overcome several problems associated with Zn anode such as particle growth, electrode pulverization, and huge volume change occurring during repeated cycling. Overall, we believe that the Zn−TiC−C nanocomposite has a great potential to be employed as an alternative anode material in LIBs and our simple and practical strategy can also be applied to explore various other nanocomposite materials for LIBs as well as Na-ion batteries.

■ ASSOCIATED CONTENT

Supporting Information

XRD patterns and SEM images of pure Zn and Zn−C composite, SEM/EDS analysis of the Zn−TiC−C nanocomposite, comparison of the initial voltage profiles of the Zn-based electrodes, and electrochemical data of the milled carbon electrode. The Supporting Information is available free of charge on the ACS Publications website at DOI: 10.1021/acsami.5b03110.

■ AUTHOR INFORMATION

Corresponding Author

*Phone: +1-512-471-1791. Fax: +1-512-471-7681. E-mail address: manth@austin.utexas.edu.

Notes

The authors declare no competing financial interest.

■ ACKNOWLEDGMENTS

This work was supported by the U.S. Department of Energy, Office of Basic Energy Sciences, Division of Materials Sciences and Engineering under Award DE-SC0005397.

■ REFERENCES

(1) Tarascon, J. M.; Armand, M. Issues and Challenges Facing Rechargeable Lithium Batteries. *Nature* **2001**, *414*, 359−367.
(2) Goodenough, J. B.; Kim, Y. Challenges for Rechargeable Li Batteries. *Chem. Mater.* **2010**, *22*, 587−603.
(3) Shen, L. F.; Uchaker, E.; Zhang, X. G.; Cao, G. Z. Hydrogenated $Li_4Ti_5O_{12}$ Nanowire Arrays for High Rate Lithium Ion Batteries. *Adv. Mater.* **2012**, *24*, 6502−6506.
(4) Zhao, L.; Hu, Y. S.; Li, H.; Wang, Z. X.; Chen, L. Q. Porous $Li_4Ti_5O_{12}$ Coated with N-Doped Carbon from Ionic Liquids for Li-Ion Batteries. *Adv. Mater.* **2011**, *23*, 1385−1388.
(5) Obrovac, M. N.; Christensen, L. Structural Changes in Silicon Anodes during Lithium Insertion/Extraction. *Electrochem. Solid-State Lett.* **2004**, *7*, A93−A96.
(6) Liu, N.; Lu, Z. D.; Zhao, J.; McDowell, M. T.; Lee, H. W.; Zhao, W. T.; Cui, Y. A Pomegranate-Inspired Nanoscale Design for Large-Volume-Change Lithium Battery Anodes. *Nat. Nanotechnol.* **2014**, *9*, 187−192.
(7) Kim, S. O.; Manthiram, A. A Facile, Low-Cost Synthesis of High-Performance Silicon-Based Composite Anodes with High Tap Density for Lithium-Ion Batteries. *J. Mater. Chem. A* **2015**, *3*, 2399−2406.
(8) Winter, M.; Besenhard, J. O. Electrochemical Lithiation of Tin and Tin-Based Intermetallics and Composites. *Electrochim. Acta* **1999**, *45*, 31−50.
(9) Yoon, S.; Manthiram, A. Nanoengineered Sn-TiC-C Composite Anode for Lithium Ion Batteries. *J. Mater. Chem.* **2010**, *20*, 236−239.
(10) Yoon, S.; Manthiram, A. Sb-MO_x-C(M = Al, Ti, or Mo) Nanocomposite Anodes for Lithium-Ion Batteries. *Chem. Mater.* **2009**, *21*, 3898−3904.

DOI: 10.1021/acsami.5b03110
ACS Appl. Mater. Interfaces 2015, 7, 14801−14807

(11) Allcorn, E.; Manthiram, A. NiSb-Al_2O_3-C Nanocomposite Anodes with Long Cycle Life for Li-Ion Batteries. *J. Phys. Chem. C* **2014**, *118*, 811−822.
(12) Allcorn, E.; Manthiram, A. High-Rate, High-Density FeSb-TiC-C Nanocomposite Anodes for Lithium-Ion Batteries. *J. Mater. Chem. A* **2015**, *3*, 3891−3900.
(13) Nitta, N.; Yushin, G. High-Capacity Anode Materials for Lithium- Ion Batteries: Choice of Elements and Structures for Active Particles. *Part. Part. Syst. Charact.* **2014**, *31*, 317−336.
(14) Zhang, W. J. A Review of the Electrochemical Performance of Alloy Anodes for Lithium-Ion Batteries. *J. Power Sources* **2011**, *196*, 13−24.
(15) Park, C. M.; Kim, J. H.; Kim, H.; Sohn, H. J. Li-Alloy Based Anode Materials for Li Secondary Batteries. *Chem. Soc. Rev.* **2010**, *39*, 3115−3141.
(16) Shi, Z.; Liu, M. L.; Gole, J. L. Electrochemical Properties of Li-Zn Alloy Electrodes Prepared by Kinetically Controlled Vapor Deposition for Lithium Batteries. *Electrochem. Solid-State Lett.* **2000**, *3*, 312−315.
(17) Bichat, M. P.; Pascal, J. L.; Gillot, F.; Favier, F. Electrochemical Lithium Insertion in Zn_3P_2 Zinc Phosphide. *Chem. Mater.* **2005**, *17*, 6761−6771.
(18) Dailly, A.; Ghanbaja, J.; Willmann, P.; Billaud, D. Electrochemical Insertion of Lithium into Graphite-Zinc Composites. *J. Appl. Electrochem.* **2004**, *34*, 885−890.
(19) Park, C. M.; Sohn, H. J. Quasi-Intercalation and Facile Amorphization in Layered ZnSb for Li-Ion Batteries. *Adv. Mater.* **2010**, *22*, 47−52.
(20) Hwa, Y.; Sung, J. H.; Wang, B.; Park, C. M.; Sohn, H. J. Nanostructured Zn-based Composite Anodes for Rechargeable Li-Ion Batteries. *J. Mater. Chem.* **2012**, *22*, 12767−12773.
(21) Applestone, D.; Manthiram, A. Cu_6Sn_5-TiC-C Nanocomposite Alloy Anodes with High Volumetric Capacity for Lithium Ion Batteries. *RSC Adv.* **2012**, *2*, 5411−5417.
(22) Kim, I. T.; Allcorn, E.; Manthiram, A. High-Performance FeSb-TiC-C Nanocomposite Anodes for Sodium-Ion Batteries. *Phys. Chem. Chem. Phys.* **2014**, *16*, 12884−12889.
(23) Kim, I. T.; Kim, S. O.; Manthiram, A. Effect of TiC Addition on SnSb-C Composite Anodes for Sodium-Ion Batteries. *J. Power Sources* **2014**, *269*, 848−854.
(24) Leibowitz, J.; Allcorn, E.; Manthiram, A. SnSb−TiC−C Nanocomposite Alloy Anodes for Lithium-Ion Batteries. *J. Power Sources* **2015**, *279*, 549−554.
(25) Jia, H. L.; Zhang, Z. H.; Qi, Z.; Liu, G. D.; Bian, X. F. Formation of Nanocrystalline TiC from Titanium and Different Carbon Sources by Mechanical Alloying. *J. Alloys Compd.* **2009**, *472*, 97−103.
(26) Yao, Y.; Huo, K. F.; Hu, L. B.; Liu, N. A.; Ha, J. J.; McDowell, M. T.; Chu, P. K.; Cui, Y. Highly Conductive, Mechanically Robust, and Electrochemically Inactive TiC/C Nanofiber Scaffold for High-Performance Silicon Anode Batteries. *ACS Nano* **2011**, *5*, 8346−8351.
(27) Mani, A.; Aubert, P.; Mercier, F.; Khodja, H.; Berthier, C.; Houdy, P. Effects of Residual Stress on the Mechanical and Structural Properties of TiC Thin Films Grown by RF Sputtering. *Surf. Coat. Technol.* **2005**, *194*, 190−195.
(28) Biesinger, M. C.; Lau, L. W. M.; Gerson, A. R.; Smart, R. S. C. Resolving Surface Chemical States in XPS Analysis of First Row Transition Metals, Oxides and Hydroxides: Sc, Ti, V, Cu and Zn. *Appl. Surf. Sci.* **2010**, *257*, 887−898.
(29) Chang, Y. H.; Chiu, H. T. Nano-Sizing Titanium into Titanium Carbide by 1-Chlorobutane. *J. Mater. Res.* **2002**, *17*, 2779−2782.
(30) Allam, N. K.; Alamgir, F.; El-Sayed, M. A. Enhanced Photoassisted Water Electrolysis Using Vertically Oriented Anodically Fabricated Ti-Nb-Zr-O Mixed Oxide Nanotube Arrays. *ACS Nano* **2010**, *4*, 5819−5826.
(31) How, G. T. S.; Pandikumar, A.; Ming, H. N.; Ngee, L. H. Highly Exposed {001} Facets of Titanium Dioxide Modified with Reduced Graphene Oxide for Dopamine Sensing. *Sci. Rep.* **2014**, *4*, 1−8, DOI: 10.1038/srep05044.
(32) Krzanowski, J. E.; Leuchtner, R. E. Chemical, Mechanical, and Tribological Properties of Pulsed-Laser-Deposited Titanium Carbide and Vanadium Carbide. *J. Am. Ceram. Soc.* **1997**, *80*, 1277−1280.
(33) Tsai, P. C.; Hwang, Y. F.; Chiang, J. Y.; Chen, W. J. The Effects of Deposition Parameters on the Structure and Properties of Titanium-Containing DLC Films Synthesized by Cathodic Arc Plasma Evaporation. *Surf. Coat. Technol.* **2008**, *202*, 5350−5355.
(34) Thotiyl, M. M. O.; Freunberger, S. A.; Peng, Z. Q.; Chen, Y. H.; Liu, Z.; Bruce, P. G. A Stable Cathode for the Aprotic Li-O_2 Battery. *Nat. Mater.* **2013**, *12*, 1049−1055.
(35) Zhu, M.; Weber, C. J.; Yang, Y.; Konuma, M.; Starke, U.; Kern, K.; Bittner, A. M. Chemical and Electrochemical Ageing of Carbon Materials Used in Supercapacitor Electrodes. *Carbon* **2008**, *46*, 1829−1840.
(36) Shin, H. J.; Kim, K. K.; Benayad, A.; Yoon, S. M.; Park, H. K.; Jung, I. S.; Jin, M. H.; Jeong, H. K.; Kim, J. M.; Choi, J. Y.; Lee, Y. H. Efficient Reduction of Graphite Oxide by Sodium Borohydride and Its Effect on Electrical Conductance. *Adv. Funct. Mater.* **2009**, *19*, 1987−1992.
(37) Suryanarayana, C.; Al-Aqeeli, N. Mechanically Alloyed Nanocomposites. *Prog. Mater. Sci.* **2013**, *58*, 383−502.
(38) Courtney, I. A.; Dahn, J. R. Key Factors Controlling the Reversibility of the Reaction of Lithium with SnO_2 and Sn_2BPO_6 Glass. *J. Electrochem. Soc.* **1997**, *144*, 2943−2948.

DOI: 10.1021/acsami.5b03110
ACS Appl. Mater. Interfaces 2015, 7, 14801−14807